SMSI-induced charge transfer for selective hydrogenolysis of polyolefins

Weilin Tu [a,1], Mingyu Chu [a,1], Xianpeng Wang [a,b,1], Xuchun Wang [a,c], Yifan Li [d], Wenxiu Yang [e], Muhan Cao [a], Lu Wang [a,*], Youyong Li [a], Tsun-Kong Sham [c], Yi Cui [d,*], Qiao Zhang [a], Jinxing Chen [a,*]

[a] Institute of Functional Nano & Soft Materials (FUNSOM), Jiangsu Key Laboratory of Advanced Negative Carbon Technologies, Soochow University, Suzhou 215123, PR China
[b] Macao Institute of Materials Science and Engineering, Macau University of Science and Technology, Taipa 999078, Macao Special Adminstrative Region of China
[c] Department of Chemistry, University of Western Ontario, London, ON N6A 5B7, Canada
[d] i-lab, Vacuum Interconnected Nanotech Workstation, Suzhou Institute of Nano-Tech and Nano-Bionics, Chinese Academy of Sciences, Suzhou 215123, PR China
[e] Analysis and testing center of Southeast University, Southeast University, Jiulonghu Lake Campus, Nanjing 211189, Jiangsu, PR China

ARTICLE INFO

ABSTRACT

The in-depth mechanism of the emerging Ru-catalyzed polyolefin hydrogenolysis remains unclear. Here, we overcome this challenge by constructing a strong metal-support interaction (SMSI) system based on Ru/TiO2 catalysts. With the increase of SMSI intensity, electrons are transferred from the TiO_x capping layer to the Ru species. This effect facilitates the key steps of hydrogenation/desorption, while having little effect on the dehydrogenation and C–C cracking elementary reactions. As a result, the catalyst with higher hydrogenation capability prone to proceed hydrogenation and desorption step, thus suppressing cascade C–C cracking and avoiding the production of low value methane. The catalyst with the strongest SMSI effect exhibits a liquid fuel yield of 89.4% at ~100% solid conversion. The SMSI effect also enables the catalysts with superior stability, so it can also efficiently upcycle commercial polyolefins. This work provides an in-depth understanding of the effects of metal-support interactions on polyolefin hydrogenolysis and paves the way for catalyst design.

1. Introduction

Ever-growing environmental pollution caused by waste plastics has become an urgent threat to modern society [1–4]. As the plastics with the highest manufacture proportion above 60% [5–7], the waste polyolefins are much more difficult to be recycled due to their high chemical inertness, resulting in low recovery efficiencies below 10% [8,9]. Given that polyolefins are essential hydrocarbons for energy needs, the waste polyolefins should be recycled timely and upgraded to value-added chemicals wherever possible [10,11].

Recently, chemical hydrogenolysis of waste polyolefins to high-valued fuels over Ru nanoparticles, one of the most efficient catalyst, holds great promise in polyolefin upcycling [12–22]. This type of reaction involves the activation of C–H bond, cracking of C–C bond, as well as hydrogenation and desorption steps, which are all related to Ru species [13,16,23,24]. Therefore, a rational catalyst design is highly required. For example, János Szanyi et al. revealed that Ru particle with

a higher disorder degree (smaller size) can suppress terminal C–C cleavage, suppressing methane production [17]. On the other hand, the metal-support interaction also affects polyolefin hydrogenolysis significantly. For instance, while the researchers are still unclear about the mechanism of the support effect, they have basically screened out that Ru catalysts supported on CeO2, TiO2, and ZrO2 showed much higher hydrogenolysis activity than those loaded on SiO2 and Al2O3 [12,18,25, 26]. These results suggest that inactive supports enable the modulation of geometric/electronic structures of Ru species, leading to the enhanced catalytic performance [27]. Vlachos et al. have recently modulated the Ru-TiO2 interaction by tuning the pH values during the impregnation process. The Ru species in the optimal catalyst possessed rich electrons and a strong hydrogen-spillover effect, which exhibits a 3-fold enhancement in hydrogenolysis rate [28]. Although efficient metal-support combinations for polyolefin hydrogenolysis can be screened out through extensive experience and experiments, in-depth mechanistic studies are still challenging because the polyolefin

---

hydrogenolysis reaction is in its infancy and many parameters are entangled with each other.

In this work, we systematically investigated the support effect on polyolefin hydrogenolysis by using Ru/TiO$_2$ as the model catalysts with tunable strong metal-support interaction (SMSI). We revealed that the SMSI effect enabled the charge transfer from the TiO$_2$ to Ru nanoparticles. Further experimental results and DFT calculations showed that these electron-rich Ru species did not promote the activation of C–H bond and cracking of C–C bond, while boosted the hydrogenation and desorption processes of olefin intermediates, avoiding the combined C–C cracking to produce methane and favor more liquid fuels. As a result, the one with the strongest SMSI effect exhibited the highest liquid fuel yield of 89.4% at close solid conversions of ~100%. The built structure-performance relationship not only gives an in-depth mechanism understanding of polyolefin hydrogenolysis but also provides new insight of catalyst design for plastic upcycling.

2. Experiment

2.1. Chemicals

Ruthenium (III) Chloride Trihydrate (RuCl$_3$·3H$_2$O, 99.9%), Sodium borohydride (NaBH$_4$, 99%), Titanium dioxide, anatase (TiO$_2$, 99.8%, particle size ~60 nm) were purchased from Alfa, Aldrich and Aladdin, respectively. Low-density polyethylene (LDPE, melting index = 20–30 g/10 min, powder size: 1000 mesh), high-density polyethylene (HDPE, melting index = 6–9 g/10 min, powder size: 200 mesh) and polypropylene (PP, M_n = 4000 ± 500) were provided from Macklin, n-hexadecane (n-C$_{16}$H$_{34}$, 99%) was purchased from Energy Chemical. The commercial LDPE flakes, PP bottle and black-PP lid were brought from Alibaba Group and cut into about 0.5 × 0.5 cm flakes for further hydrogenolysis.

2.2. Synthesis of Ru/TiO$_2$-HX catalysts

In a typical synthesis, the Ru/TiO$_2$ catalyst was prepared by a NaBH$_4$ reduction method. 1.9 g of commercial anatase TiO$_2$ was dispersed in 20 mL deionized water in a beaker A, and 0.2857 g RuCl$_3$3 H$_2$O dissolved in 20 mL deionized in another beaker B, then dropped the solution into beaker A and stirred at 400 rpm for 3.5 h. Afterward, 252.6 mg NaBH$_4$ dissolved in 5 mL deionized water was dropped into the above mixture, followed by stirring for 30 min. The Ru/TiO$_2$ catalyst was washed by centrifugation with water and dried overnight in an oven at 80 °C. The Ru/TiO$_2$-HX (X represents the reduction temperature, X = 300, 400, 500, 600 °C) catalysts were prepared by reducing Ru/TiO$_2$ catalyst in a H$_2$/Ar flow (80 mL/min) at different temperatures for 2 h.

2.3. Evaluation of hydrogenolysis performance

The catalytic performance of polyolefin hydrogenolysis was evaluated in a 100 mL batch stainless-steel autoclave. Typically, 50 mg catalyst and 2 g polyolefin were first physically mixed and then placed at the bottom of the reactor. Before heating the reaction, the reactor needed to be pre-flushed with high-pressure H$_2$ for at least 3 times and finally kept at 2 MPa. The stirring rate was kept at 400 rpm in this work. After the reaction was completed, the reactor was cooled to room temperature, a gas sampling bag was used to collect the gaseous products. The gaseous products were analyzed by a gas chromatograph (GC) with flame ionization detector (FID), the model of capillary-column is TM-Al$_2$O$_3$. On the other hand, the solid residue and liquid products were dispersed and dissolved in 30 mL toluene, followed by the separation via refrigerated centrifugation. The solid residue was washed by n-hexane and put into oven to dry overnight at 80 °C. The liquid products were analyzed by another GC-FID with a capillary-column model of HP-1. The solid conversion and yields of gaseous/liquid products were calculated by the following equations:

$$Solid \quad conv.(\%) = \left(1 - \frac{m(residuals) - m(catalyst)}{m(plastic)}\right) \times 100\%$$

$$Product \quad yield \quad (\%) = \frac{n(C \quad in \quad C_x \quad product)}{n(C \quad in \quad initial \quad polyolefin)} \times 100\%$$

2.4. Evaluation of hydrogenation performance

The propylene hydrogenation reaction was performed using a fixed quartz reactor (inner diameter: 8 mm). The catalyst was physically mixed with quartz sand (60–80 mesh) with a weight ratio of 1:3 and then put them in the middle of the reactor. Propylene, hydrogen and nitrogen were introduced by three mass flow controllers. The input and output hydrocarbons were detected by the GC-FID using a TM-Al$_2$O$_3$ capillary-column, H$_2$ and N$_2$ were measured by the thermal conductivity detector (TCD) using a packed column with the model of TDX-01. The TOF values was calculated by the following equation:

$$Con. = \frac{n(C_3H_6)_{in} - n(C_3H_6)_{out}}{n(C_3H_6)_{in}} \times 100\%$$

$$STY_{C3H6} = \frac{m(C_3H_8)}{m(Ru_{active}) \times t}$$

2.5. Evaluation of n-hexadecane hydrogenolysis performance

The n-hexadecane hydrogenolysis experiments were conducted in a 100 mL batch stainless-steel autoclave, the catalyst was put in the bottle of reactor, followed by the pre-flush using H$_2$ for 3 times and maintained at 2 MPa. The stirring rate was kept at 400 rpm in this work. After the reaction was completed, the reactor was cooled to room temperature, the gases were collected by a gas sampling bag. The gaseous and liquid products were analyzed by GCs with FID (TM-Al$_2$O$_3$) and FID (HP-1), the content of H$_2$ was analyzed by TCD (TDX-01), respectively. The number of C-C cracking is calculated by the amount of end groups of the products. The conversion of n-hexadecane and STY of the moles of C-C cracking was calculated by the following equation:

$$Conv. = \frac{n(C_{16}H_{34})_{before} - n(C_{16}H_{34})_{after}}{n(C_{16}H_{34})_{before}} \times 100\%$$

$$STY_{C-C} = \frac{2 \times \sum_1^{16} n(C_nH_{2n+2}) - 2 \times n(C_{16}H_{34})_{before}}{m(Ru_{active}) \times t \times 2}$$

2.6. Stability test

In polyolefins hydrogenolysis, the collected solid residuals including the solid products and catalyst were dispersed in a hot toluene solution to dissolve the hydrocarbons, followed by the centrifugation of the hot solution to separate the catalyst. Repeat the above process five times, then dry the catalyst overnight at 80 °C for further use. In general, there is a 10–20% mass loss in each recovered catalyst, which will be supplemented with fresh catalyst for the next cycle.

The n-butane hydrogenolysis reaction was performed using a fixed quartz reactor with an inner diameter of 10 mm. The catalyst was physically mixed with quartz sand (60–80 mesh) and the mass ratio is 20: 1000, and then the mixture was placed in the middle of the reactor. Under the nitrogen atmosphere (40 mL/min), the reactor temperature was gradually increased from 25 to 250 °C. Subsequently, hydrogen (30 mL/min) and n-butane (3 mL/min) were introduced by mass flow controllers. The output hydrocarbons were detected by GC-FID using a TM-Al$_2$O$_3$ capillary-column. The conversion of n-butane was calculated by the following equation:

$$Conv. = \frac{n(C_4H_{10})_{in} - n(C_4H_{10})_{out}}{n(C_4H_{10})_{in}} \times 100\%$$

2.7. Characterizations

Inductivity coupled plasma optical emission spectrometry (ICP-OES: Thermo Fisher iCAP PRO) was used to determine the elemental composition. Powder X-ray diffraction (XRD) patterns were acquired using an analytical Empyrean machine at 40 kV and 40 mA. TEM, STEM, HR-TEM and corresponding elemental mapping images were tested by the field emission high-resolution transmission electron microscopy (FEI Talos F200X, Thermo Fisher) from Southeast University. The H_2-temperature-programmed desorption (H_2-TPD) and H_2-temperature-programmed reduction (H_2-TPR) were detected by an automatic chemical adsorption instrument (FINETEC/FINE-SORB-3010). For H_2-TPD, 30 mg as-prepared catalyst was put into a U-shape quartz tube, following by four steps: (1) Ar pre-flushing to remove the physically adsorbed gases, (2) exposing the sample to the adsorbate flow, (3) Ar flushing to remove the physically adsorbed adsorbate and (4) desorption by heating in Ar. For H_2-TPR, 10 mg catalyst was put into a U-shape quartz tube, following by two steps: (1) Ar pre-flushing to remove the physically adsorbed gases, (2) heating from room temperature to 620 °C in a H_2/Ar flow. The outlet H_2 was detected by a TCD with the current and temperature of 90 mA and 60 °C. The NAP-XPS spectra were measured by a customized end station from SPECS consisting of a NAP-XPS chamber in the Vacuum Interconnected Nanotech Workstation in
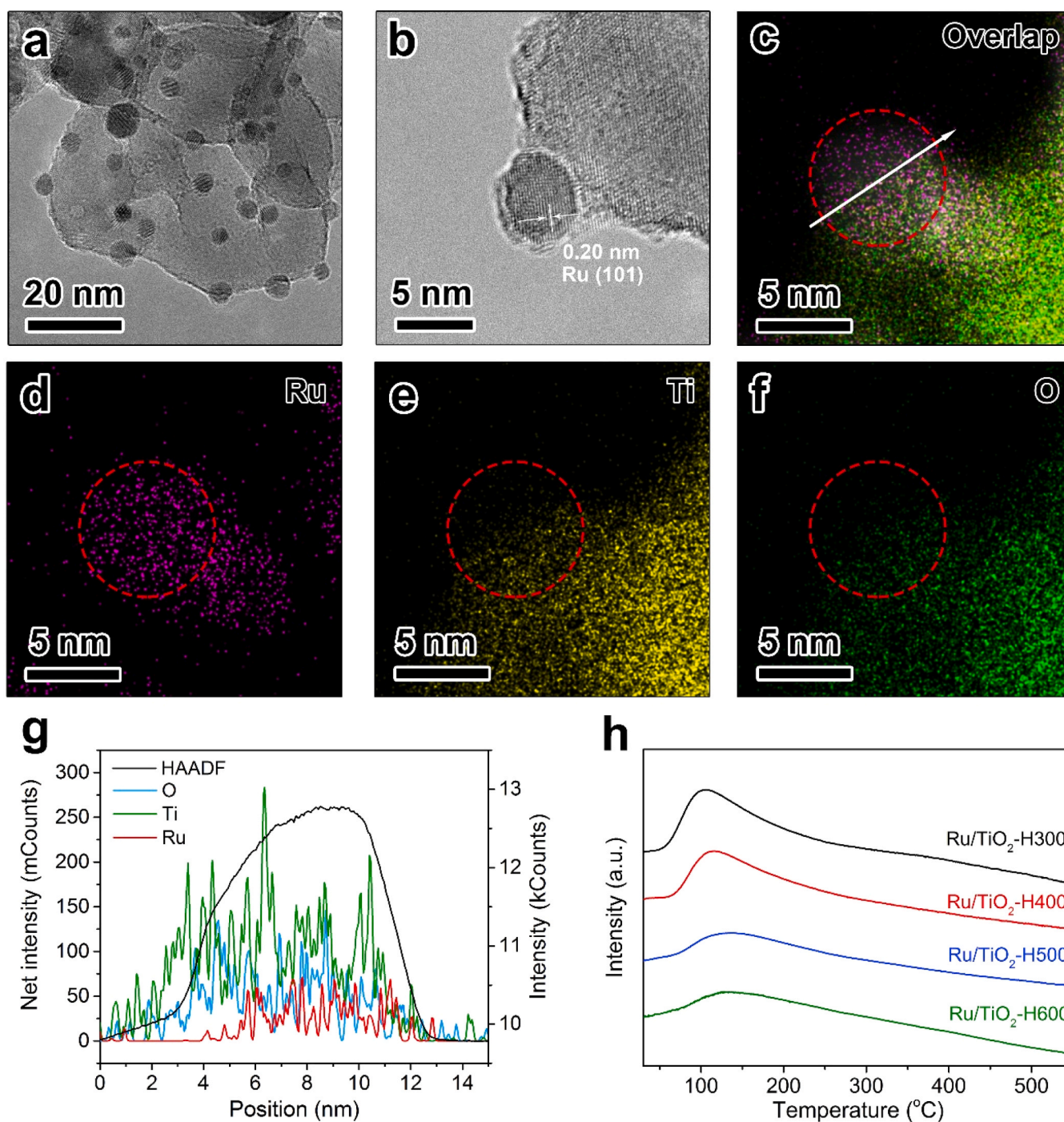
Fig. 1. Structural characterizations of Ru/TiO$_2$-HX catalysts. (a) TEM, (b) high-resolution TEM and (c) elemental mapping images of Ru/TiO$_2$-H600 catalyst. (d) Ru, (e) Ti and (f) O elemental distributions and (g) corresponding linear scanning result. (h) H_2-TPD results of Ru/TiO$_2$-HX catalysts.

Suzhou (Nano-X). In situ NAP-XPS measurement was performed on a SPECS NAP-XPS instrument with a temperature-controllable laser heating device and thermocouple equipped. The photon source is the monochromatic X-ray source of Al Kα (1486.6 eV). The catalyst powder was pressed onto copper foam, and then the sample was fixed onto the XPS sample holder by tantalum strips. In a routine test, Ru 3d, O 1 s, and Ti 2p spectra were collected under UHV at 25 °C, followed by the heat-treatment of the sample using the laser at 300, 400, 500, or 600 °C in a pure hydrogen atmosphere (0.2 mbar) for 5 min. The BE was corrected by using O 1 s due to the overlap of C 1 s and Ru 3d signal. X-ray absorption near-edge structure (XANES) spectra were performed at Ru L_3-edge using a fluorescence yield (FY) mode at the 20 BM beamline of the Advanced Photon Source (APS) operated by Argonne National Laboratory, United States.

3. Results and discussions

3.1. Catalyst synthesis and characterizations

The SMSI, initiated by Tauster in the 1970 s [29], is the phenomenon in which reducible support would encapsulate metal nanoparticles supported on its surface after being treated with hydrogen at high temperatures. It is usually accompanied by charge transfer and interfacial perimeter changes [30,31]. Hence, SMSI is a unique and efficient strategy to modulate catalyst performances, including activity, selectivity, and stability [32–38]. To obtain Ru catalysts with tunable SMSI intensity, we first synthesized pristine Ru/TiO$_2$ catalyst with 4.74 *wt.*% Ru loading (measured by inductively coupled plasma optical emission spectroscopy, ICP-OES) via a solution reduction method [39], in which a NaBH$_4$ solution was injected to the aqueous solution containing TiO$_2$ nanoparticles and RuCl$_3$. These Ru/TiO$_2$ catalysts were then subjected to H$_2$ reduction at different temperatures for 2 h to trigger the SMSI effect. The catalysts were named as Ru/TiO$_2$-HX (X represents reduction temperature, = 300, 400, 500, 600 °C). Regardless of treating temperature, the Ru nanoparticles (Ru NPs) in four samples all are well dispersed on the surface of TiO$_2$ with an average size ~4.5 nm (Fig. 1a and Fig. S1–S2). The neglectable size fluctuation indicates that TiO$_2$ has a strong anchoring effect to Ru nanoparticles so that the surface migration and agglomeration is prevented even after high temperature treatments [40]. The four catalysts exhibit similar X-ray diffraction (XRD) peaks of anatase TiO$_2$ (PDF#21–1272), as well as the weak *hcp* Ru peaks (PDF#06–0663), which confirm the small size and high dispersion of Ru NPs again (Fig. S3).

In order to better observe the SMSI-induced encapsulation of Ru surface by TiO$_2$, Ru/TiO$_2$-H600 was selected as represent for high-resolution transmission electron microscopy (HR-TEM) measurement. As shown in Fig. 1b, a clear lattice fringe of 0.20 nm is observed and indexed to the (101) facet of *hcp* Ru. More importantly, an amorphous coating layer of TiO$_x$ can be observed at the interface between Ru and TiO$_2$, which can be further confirmed by STEM-EDX (Fig. 1c-f). In the red-dotted region, the elemental distributions of Ti (yellow) and O (green) are at the Ru-TiO$_2$ interface and partially around the Ru NPs, coupled with the elemental line-scanning results (Fig. 1g), all confirm the SMSI-induced encapsulation.

The encapsulation degree of catalysts treated at different reduction temperatures was further quantified by H$_2$-programmed desorption (H$_2$-TPD) and H$_2$-programmed reduction (H$_2$-TPR). The desorption peaks ranged around 100–150 °C are corresponding to the H$_2$ adsorbed on the surface of Ru NPs in H$_2$-TPD [38,41] (Fig. 1h) and the signal observed below approximately 100 °C in the H$_2$-TPR spectrum can be attributed to the reduction of Ru species (Fig. S4). The increase of reduction temperature favors for the formation of interfacial TiO$_x$ to encapsulate Ru NPs (Fig. S2d-S2f). As a result, the number of exposed Ru sites decreases, which is also reflected in the gradual decrease in the amount of H$_2$ adsorption in H$_2$-TPD and the decrease in the area of the H$_2$ consumption peak in H$_2$-TPR. The surface Ru dispersions of various catalysts show a gradual decrease from 20.4% to 9.4% calculated by the adsorbed H$_2$ amounts (Table S1). It should be noted that the theoretical dispersion of Ru NPs with an average size of ~4.5 nm is 24.9%, which suggests that a 300° C reduction condition has already initiated the SMSI effect.[36] More importantly, as the SMSI effect enhanced, the H$_2$ desorption peak gradually shifts from ~106 °C (Ru/TiO$_2$-H300) to ~134 °C (Ru/TiO$_2$-H600), indicating that the SMSI effect assists to improving H$_2$ adsorption strength on Ru NPs. In addition, the shift of the H$_2$ consumption peak towards higher temperatures also suggests that a stronger interaction between Ru and the support makes the reduction of Ru more challenging (Fig. S4). Typically, a high-temperature peak is observed in the H$_2$-TPD spectrum **due to the desorption** of hydrogen spillover [42]. However, all catalysts exhibit only a low-temperature peak which can exclude the effect of hydrogen spillover. These observations align with the changes in TPD and TPR signals commonly associated with the classic SMSI effect and this unique phenomenon can promote the hydrogenation step of the Ru/TiO$_2$ catalyst in the polyolefin hydrogenolysis (see detailed discussion in the catalytic mechanism section).

3.2. SMSI-induced charge transfer

In a classic SMSI system, the encapsulation is usually accomplishment with charge transfer between metal and support. To probe the electronic states of Ru, Ti and O species, in-situ Near-ambient-pressure X-ray photoelectron spectroscopy (NAP-XPS) was performed because Ru NPs tend to be oxidized during ex-situ tests (Fig. 2a). As presented in Fig. 2b of the Ru 3d$_{5/2}$ spectrum, the Ru species in pristine Ru/TiO$_2$ are mainly in the form of Ru^{4+} (280.7 eV). After in-situ heating at 300 °C in H$_2$ atmosphere, the Ru^{4+} species were reduced to metallic Ru^0 (280.2 eV). Further increasing the reduction temperature caused a gradually shift of Ru^0 position to lower binding energy at 279.7 eV (Ru/TiO$_2$-H600), suggesting the occurrence of the electron transfer from support to metal [31]. In addition, there were three O species can be analyzed and fitted in O 1 s spectrum (Fig. 2c). The O species in pristine Ru/TiO$_2$ catalyst exhibit most metal–oxygen (M–O) bonds and few O–H bonds caused by adsorbed H$_2$O. As the reduction temperature increase, the dehydration process eliminated the O–H signal. At the same time, an oxygen vacancies (O$_v$) signal appeared, and the O$_v$ content increases from ~4.5% in Ru/TiO$_2$-H300 to ~9.2% in Ru/TiO$_2$-H600 (Table S2). Such an effect is incline to TiO$_x$ structure at Ru-TiO$_2$ interface, consistent with the typical SMSI effect. In contrast to significant changes in Ru 3d$_{5/2}$ and O 1 s signals, the Ti species mainly existed in the form of Ti^{4+} (Fig. S5), which may be caused by low loading amount of Ru.

X-ray absorption near-edge structure (XANES) at Ru L_3-edge, collected with a bulk-sensitive fluorescence yield (FY) detection mode, was further used to track the change in the electronic structure of Ru (Fig. 2d). Here, Ru thin film and RuO$_2$ powder were used as references, but their spectra were collected with a total electron yield (TEY) detection mode considering the server self-absorption of FY mode for thick samples. The spectra of Ru/TiO$_2$ samples show a similarity with that of Ru thin film, indicating that Ru is mainly existing in the metallic state. XANES probes the unoccupied state of materials, of which the first sharp peak above the edge jump (2p$_{3/2}$→4d transition) is known as the whiteline. As shown in Fig. 2d, the whiteline of Ru/TiO$_2$ catalysts shrinks with increasing the reduction temperature, suggesting that Ru gains *d* electrons since the area under the whiteline is proportional to the number of valence holes. Fig. 2e shows the fitting profiles of the whiteline by subtracting an arctangent background (black dotted lines in Fig. 2e). The integrated area (A$_{WL}$) under the whiteline decreases from 13.41 to 11.67 upon increasing the reduction temperature, which precisely confirms the variation in the electronic structure of Ru. XANES results are in good accord with the NAP-XPS observation, both providing solid evidence for the existence of SMSI.
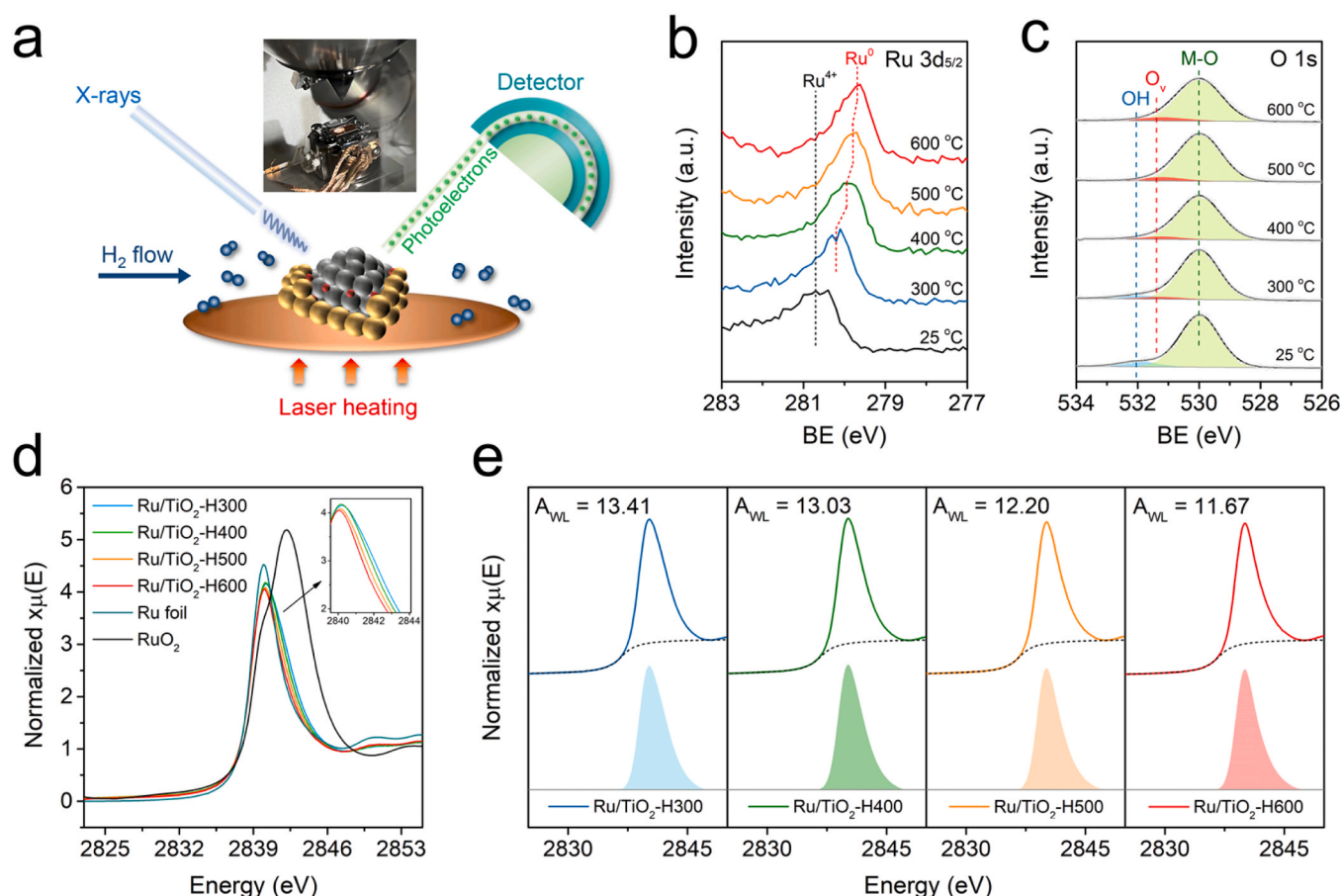
Fig. 2. Electronic structures of Ru/TiO₂-HX catalysts. (a) Schematic diagram and picture of the NAP-XPS test process. (b, c) NAP-XPS spectra of (b) Ru $3d_{5/2}$ orbital and (c) O 1 s orbital. (d) XANES spectra of Ru/TiO₂-HX catalysts at Ru L_3-edge. The Ru foil and RuO₂ were used as references. (e) The whiteline fitting of Ru/TiO₂-HX catalysts.

3.3. PE hydrogenolysis over Ru/TiO₂-HX

The polyolefin hydrogenolysis experiments were conducted in a 100 mL batch stainless-steel autoclave, capped with two pressure sensors and a temperature monitor. The time-dependent low-density polyethylene (LDPE) hydrogenolysis experiments over all Ru/TiO₂-HX catalysts were first explored to investigate the effects of SMSI on the catalytic reaction. In detail, the catalyst/LDPE ratio was kept at 50 mg/ 2000 mg and the H₂ pressure was set to 2 MPa. As shown in Fig. 3a, LDPE conversion dropped because of the less exposed Ru site due to the SMSI degree increase which shows the similar trend in hydrogenolysis of alkanes [43,44]. More specifically, the Ru/TiO₂-H300 possesses the highest reaction rate with solid conversion of 98.4% in 1.5 h, while the Ru/TiO₂-H600 possesses the lowest solid conversion of 48.5%. For Ru/TiO₂-H300, the gaseous (mainly low value CH₄) yield increased from 15.5% to 37.0% while the reaction time was increased to 4 h (Fig. 3b). The drastic increase in short-chain gaseous alkanes indicates that further increasing the reaction time to increase conversion rate also induced over-hydrogenolysis of long-chain liquid fuels. Nevertheless, the growth rates in gas yield over time (the fitted slope of the increase in gas yield over time) showed a deceleration. For example, the Ru/TiO₂-H600 with the strongest MSI effect has the lowest gas yield of 8.6% and the highest liquid fuel yield of 89.4% (Fig. S6) when the solid conversion is at 98.0%.

To better compare the effects of SMSI on polyolefin selective hydrogenolysis, we regulate these catalysts under similar solid conversions ranged in 95 − 99% by adjusting the reaction time (Fig. 3**c**). As the enhanced SMSI effect from Ru/TiO₂-H300 to Ru/TiO₂-H600, the value-

added liquid yields displayed a continuing upward trend from 77.0% to 86.9%, in contrast to the continuous decline in gas yields (from 21.4% to 8.03%). To eliminate the impact of excessive reactions, the reactions at lower conversion level of approximately 45% solid conversion were compared between Ru/TiO₂-H600 and Ru/TiO₂-H300 (Fig. S7). The results consistently demonstrate the same trend observed at high conversion levels. Specifically, Ru/TiO₂-H300 consistently demonstrate a higher gas yield (6.48%) than **Ru/TiO₂-H600** (2.92%), while **Ru/TiO₂-H600** is more inclined towards the production of liquid products. These findings further support and validate the change of selectivity due to the SMSI effect. In addition, the liquid product distribution exhibit diversity over catalysts with different SMSI degree. Accordingly, the product distributions on Ru/TiO₂-H300 and Ru/TiO₂-H600 under 3.5 h reaction time showed two distinct differences (Fig. 3d-e). The liquid products were more in the form of jet fuel (56.3%) and kerosene (57.5%) for Ru/ TiO₂-H300 and diesel (53.8%) and motor oil (51.7%) for Ru/TiO₂-H600, respectively. In other reaction times and catalysts with different SMSI also showed diverse product distributions (Fig. S8), further illustrating the regulation of product distribution. This diversity of products distribution at same reaction time or same conversion indicated that catalyst structure plays a crucial role in regulation product distribution. More specifically, the product distribution can be controlled by adjusting the structure of catalyst via SMSI, and the products of Ru/TiO₂-H600 have the larger alkane numbers than that of Ru/TiO₂-H300. This trend suggests that the SMSI effect in the catalyst favored the formation of liquid products and suppresses the formation of short-chain gases (Table S3).
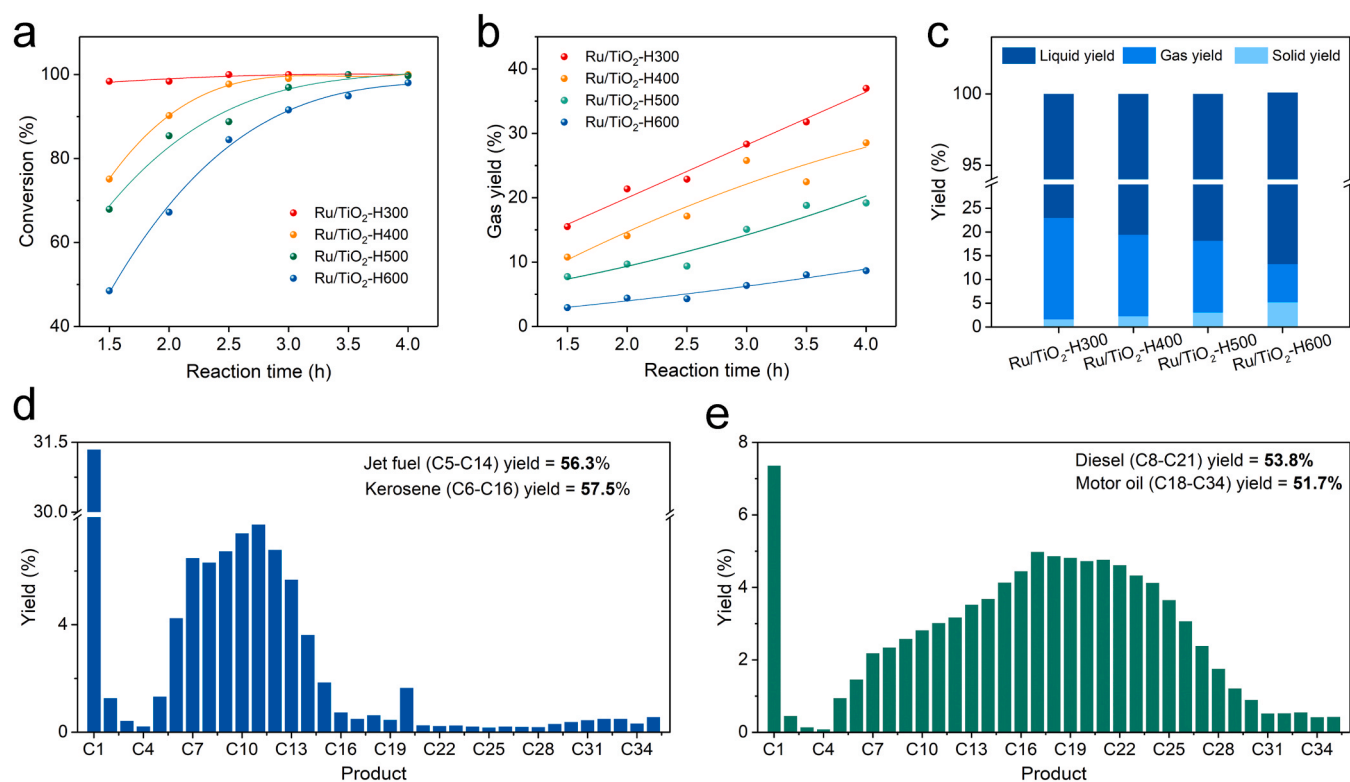
Fig. 3. Catalytic LDPE hydrogenolysis over Ru/TiO$_2$-HX catalysts. The (a) solid conversions, (b) gas yields of Ru/TiO$_2$-HX catalysts from 1.5 to 4 h of reaction time. (c) Catalytic performance of Ru/TiO$_2$-HX under the similar solid conversions. The products distribution of (d) Ru/TiO$_2$-H300 and (e) Ru/TiO$_2$-H600 when reaction time is 3.5 h. Reaction conditions: T = 240 °C, P_{H2} = 2 MPa, stirring rate = 400 rpm and m(catalyst)/m(LDPE) = 50 mg/2000 mg.

3.4. Mechanism study by probing reactions

The elementary reaction steps of polyolefin hydrogenolysis include (1) C–H activation, (2) C–C cracking and (3) hydrogenation/desorption. Among them, C–H activation is always coupling with C–C cracking and coke formation [45], complicates the product distribution. Furthermore, C–H activation is a structure-insensitive reaction [46], and we hence only designed two elementary reactions, i.e. C–C cracking and hydrogenation, to evaluate the catalytic mechanism over two catalysts. In detail, the adsorbed alkane prefer to form carbon-metal bonds after dehydrogenation and subsequent C–C bond cracking, hydrogenation and desorption in alkane hydrogenolysis [47]. Therefore, it is difficult to mimic the real hydrogenation and desorption in alkane hydrogenolysis. Here we design a reaction of propylene hydrogenation to evaluate the hydrogenation ability of catalysts, which can reflect hydrogenation in polyolefin hydrogenolysis. In addition, *n*-hexadecane hydrogenolysis was also applied to quantify the number of C–C cleavages because the products are much easier to identify. To properly compare the catalytic performance, the catalyst feeding keeps the same number of active sites calculated by H$_2$-TPD (Table S1). During the polyolefin hydrogenolysis, two possible reaction paths may occur after C–H and C–C bond cleavage of alkane molecules on the catalyst surface. The first one is hydrogenation and subsequent desorption, resulting in the generation of smaller alkanes. Another path involves further C–C bond cascade cleavage, followed by hydrogenation to form methane [13] Therefore, the catalyst's hydrogenation capacity primarily influences the selectivity of products rather than its overall catalytic activity. To probe the effect of SMSI on the hydrogenation step, we used propylene hydrogenation to evaluate hydrogenation ability of catalysts (Fig. 4a). Under the same reaction conditions and active Ru numbers, the Ru/TiO$_2$-H600 shows much higher propylene conversion of 10.2% and STY of 154.4 g$_{C3H8}$/g$_{active\ Ru}$/h than those of Ru/TiO$_2$-H300. The enhanced performance suggests that the electron-rich Ru/TiO$_2$-H600 favors the

hydrogen dissociation, thus boosting hydrogenation rate [48]. The above results indicate that the Ru/TiO$_2$-H600 with higher hydrogenation ability may be more prone to proceed hydrogenation and desorption path rather than further C–C bond cascade cleavage, which can explain the higher yield of liquid fuel in polyolefin hydrogenolysis over Ru/TiO$_2$-H600.

Another key reaction is C–C cracking which is the rate-determining step in hydrogenolysis of polyolefins, which primarily affects the catalytic activity. As shown in Fig. 4b, both catalysts share the *n*-hexadecane conversion nearly 30%. However, Ru/TiO$_2$-H300 exhibits a higher STY of 92.89 n$_{c-c}$/g$_{active\ Ru}$/h than Ru/TiO$_2$-H600, which means more C–C cleavage on the Ru/TiO$_2$-H300. The difference in the C–C cleavage number may be caused by the hydrogenation capability rather than C–C cracking capability due to the same conversion of *n*-hexadecane. The strong hydrogenation capability in Ru/TiO$_2$-H600 inhibits the continuous cascade cracking of C–C, resulting in a decrease in the number of C–C cleavage. This speculation is consistent with the regularity that Ru/TiO$_2$-H600 has a lower methane yield in the *n*-hexadecane hydrogenolysis (Fig. S9).

3.5. Mechanism study by DFT calculations

To gain deep insights into the SMSI effect on polyethylene selective hydrogenolysis on Ru/TiO$_2$ catalysts, the density functional theory (DFT) calculations were performed. According to the experimental observations, we have constructed two structural models and compared their catalytic activities: one is Ru$_3$ cluster anchored on the perfect TiO$_2$ surface (Ru$_3$/p-TiO$_2$), while the other is Ru$_3$ cluster anchored on the defective TiO$_2$ with surface oxygen vacancies (Ru$_3$/v-TiO$_2$). The three Ru atoms form a triangle Ru$_3$ cluster on both two surface models, but they exhibit distinguished electronic properties due to the different local structures and chemical environments. In Ru$_3$/p-TiO$_2$, three Ru atoms in Ru$_3$ are bonded with four O atoms and three Ti atoms from TiO$_2$ surface
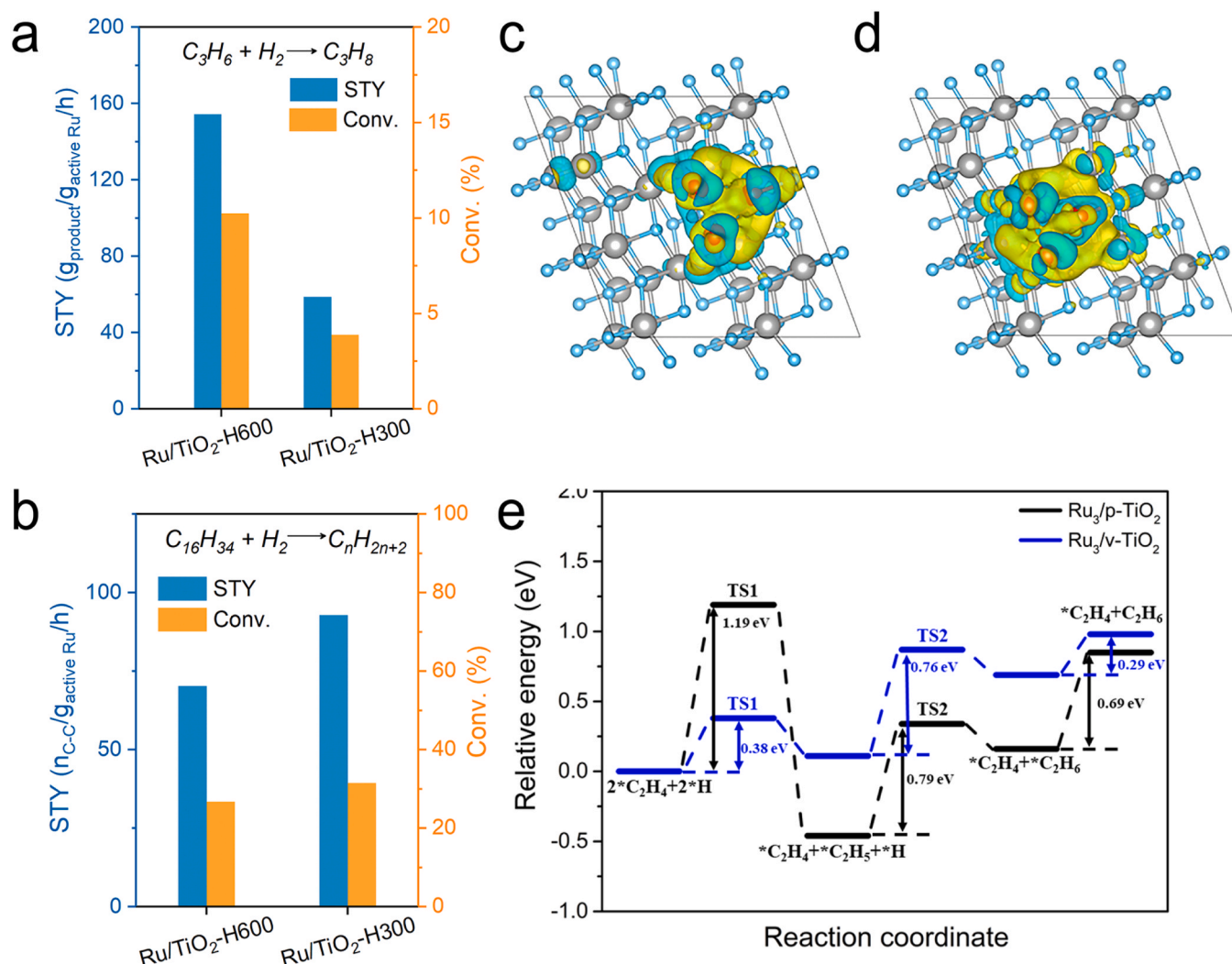
Fig. 4. Proposed mechanism analysis of PE hydrogenolysis impacted by SMSI. (a) propylene hydrogenation and (b) *n*-hexadecane hydrogenolysis. Reaction conditions: (a) $C_3H_6/H_2/N_2$ = 3/30/27 mL/min, T = 200 °C, P_{total} = 0.1 MPa, m (active Ru) = 0.23 mg; (b) m (*n*-hexadecane) = 2 g, m (active Ru) = 0.20 mg, P_{H2} = 2 MPa, stirring rate = 400 rpm, T = 200 °C, t = 20 min (c) The top views of charge density difference of $Ru_3/p-TiO_2$ and (d) $Ru_3/v-TiO_2$. (e) Density functional density (DFT) calculations of hydrogenation processes on $Ru_3/p-TiO_2$ (black) and $Ru_3/v-TiO_2$ (blue).

with the Ru-O bond lengths of ~1.97 Å. In $Ru_3/v-TiO_2$, Ru_3 cluster are connected to four Ti atoms and three O atoms with the Ru-Ti bond lengths of ~2.69 Å. Different bonding environments of Ru atoms on $Ru_3/p-TiO_2$ and $Ru_3/v-TiO_2$ surfaces lead to distinctive electronic properties. As shown in Fig. 4c-d, we have calculated the charge density difference of **$Ru_3/p-TiO_2$** and **$Ru_3/v-TiO_2$**, respectively. The Ru in **$Ru_3/v-TiO_2$** is more negatively charged than that in **$Ru_3/p-TiO_2$**. The Bader charge distributions and projected density of states (PDOS) of Ru atoms in **$Ru_3/p-TiO_2$** and **$Ru_3/v-TiO_2$** surfaces have further proved it, which is shown in Fig. S10. In $Ru_3/p-TiO_2$, the Ru atoms transfer the electrons to the surface O atoms, and the charge values on these three Ru atoms are calculated to be + 0.20 e, + 0.20 e and + 0.35 e, respectively. On the other hand, the Ru atoms in $Ru_3/v-TiO_2$ possess the more negative charge values of − 0.37 e, + 0.02 e and + 0.02 e, respectively, indicating the Ru atoms accept electrons from the surface Ti atoms. The negative charge values of Ru in $Ru_3/v-TiO_2$ show a relatively lower valence state than Ru in $Ru_3/p-TiO_2$, which is further proved by the PDOS results with the electron density of states of Ru *d*-orbital moving closer to the Fermi level (Fig. S10c). The above results suggest that our $Ru_3/v-TiO_2$ model provides an electron-rich state of active Ru by introducing the surface vacancies, which agrees well with the experiments and is suitable for further studying the catalytic mechanism.

As shown in Fig. 4e and S11–12, the reaction pathways of polyolefin hydrogenolysis on $Ru_3/p-TiO_2$ and $Ru_3/v-TiO_2$ surfaces have been investigated. For simplification, small alkanes were used to replace polyolefin molecules in the simulation [49,50], hence, *n*-butane (C_4H_{10}) is employed to simulate the polyethylene during the reaction process. First, the dehydrogenation reactions on the middle C2 and C3 atoms of C_4H_{10} on both $Ru_3/p-TiO_2$ and $Ru_3/v-TiO_2$ surfaces are calculated, and the reaction barriers are all smaller than 0.33 eV, indicating the dehydrogenation process is easy to occur. After that, the middle C2-C3 bond is preferable to break into two *$CHCH_3$ fragments with the activation barrier of 1.56 eV on $Ru_3/v-TiO_2$, which is slightly smaller than that on $Ru_3/p-TiO_2$. Next, the unsaturated C atom in *$CHCH_3$ is prone to adsorb the surface H atoms to achieve the hydrogenation process and finally desorb from the catalyst surface. On $Ru_3/p-TiO_2$ surface, the hydrogenation of *$CHCH_3$ into *CH_2CH_3 needs to overcome an activation barrier of 1.19 eV and the further hydrogenation barrier of *CH_2CH_3 into *C_2H_6 is reduced to 0.79 eV. On $Ru_3/v-TiO_2$ surface, the active site is located around the Ru2 atom with the negative charge. The hydrogenation barrier for *$CHCH_3$ to form *CH_2CH_3 is calculated to be only 0.38 eV, greatly lower than that on $Ru_3/p-TiO_2$, and the further hydrogenation barrier is 0.76 eV to obtain *C_2H_6. Moreover, the adsorbed *C_2H_6 would desorb from the catalyst surface with the smaller desorption barrier of

0.29 eV on Ru$_3$/v-TiO$_2$, inhibiting to the further C–C cracking. Therefore, the defective TiO$_2$ substrate could significantly modify the electronic property of the supported Ru nanoparticles into an electron-rich state by strong charge transfer between Ru and Ti metals, which accelerates the hydrogenation and desorption process for polyolefin hydrogenolysis, and finally resulting in the high selectivity toward liquid fuels.

In short, we proposed the effect of SMSI on polyolefin hydrogenolysis. The polyolefin molecule processed a dehydrogenation and adsorption step to bond with Ru, primarily. The C–C cleavage was then initiated to form two alkane intermediates, which have two end-of-life paths by either hydrogenation and desorption or repeating the dehydrogenation and C–C cleavage. As a result, value-added liquid fuels were formed in the first case, while methane, via cascade C–C cleavages was produced in the latter one. In addition, the two catalysts showed similar C–C cracking ability and the catalyst with a SMSI effect showed a stronger capability of hydrogenation. The result means also that electron-rich Ru NPs hold stronger hydrogenation ability, the C–C cracking was suppressed, thus favoring the formation of liquid fuels. Therefore, the regulation of the SMSI effect provides an opportunity to control product distributions for various application scenarios.

3.6. Stability tests and demonstration

Catalyst stability and recoverability are important industrial standard parameters. The SMSI effect can also stabilize the metal particles by encapsulation with the support, prevent their agglomeration in the reaction, and improve the stability of the catalyst [40]. Here, Ru/TiO$_2$-H600 with the strongest degree of SMSI was selected to study the stability in polyolefin hydrogenolysis. In detail, after one cycle of catalytic reaction, the solid residues composed of the spent catalyst and solid polymers were dissolved in hot toluene and then centrifuged to remove the polymers. The above purification processes were repeated five times to ensure catalysts were sufficiently clean. The catalyst recovery was about 80% after the purification, and the lost catalysts were supplied with fresh ones in the next test cycle. As shown in Fig. 5a, the solid conversions for five reaction cycles are all above 90%, suggesting that the Ru/TiO$_2$-H600 possesses satisfactory stability after the hydrogenolysis process. In addition, these Ru NPs were well dispersed on TiO$_2$ support with an average diameter of ~4.57 nm after 5 consecutive cycles (Fig. 5b and c), which is similar to that of the fresh catalyst (4.53 nm), confirming the good structure stability. In addition, the catalyst durability was also tested by using the hydrogenolysis of *n*-butane hydrogenolysis as the model reaction (Fig. S13). The catalytic activity of Ru/TiO$_2$-H600 remained the stable n-butane conversions of ~35.2% within long-term reaction time of 690 min. The high stability should be attributed to the encapsulation of support on Ru NPs induced by the SMSI effect.

n addition, hydrogenolysis of commercial polyolefin is another important aspect to measure the universality of catalysts, thus, several real-world polyolefins composed of LDPE, HDPE and PP, etc. were catalyzed over Ru/TiO$_2$-H600 catalyst. As shown in Fig. 5d, the catalyst with the strongest MSI effect exhibits liquid yields of above 80% for PE,
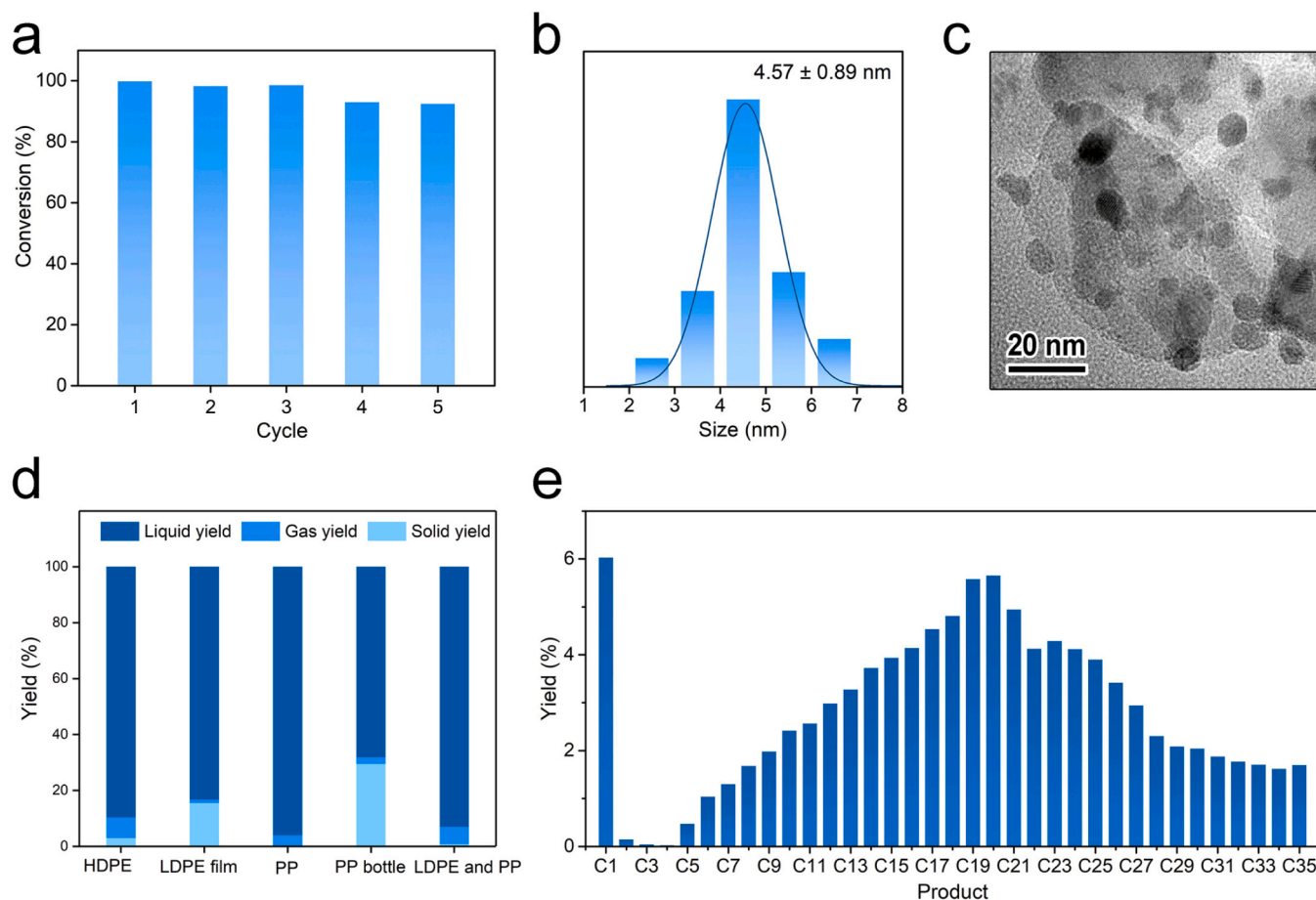
Fig. 5. Hydrogenolysis of commercial polyolefins and catalyst stability of Ru/TiO$_2$-H600. (a) Stability and recoverability test for LDPE hydrogenolysis over Ru/TiO$_2$-H600. (b) Size distribution of Ru NPs and (c) TEM image of the spent Ru/TiO$_2$ catalyst. (d) The catalytic performance of commercial polyolefin hydrogenolysis. (e) The non-solid product distribution of hydrogenolysis of LDPE + PP mixture. Conditions: T = 240 °C except reaction temperature for PP and PP bottle hydrogenolysis is 250 °C, P_{H2} = 2 MPa, reaction time is 3 h, 4 h, 12 h, 16 h and 10 h for HDPE, LDPE film, PP, PP bottle and the mixture of LDPE and PP, respectively. Specially, the mass ratio of LDPE and PP is 2:1.

and gas yields of below 8% for all plastics. Remarkably, under the same reaction conditions, the solid conversions of HDPE and LDPE hydrogenolysis are 97% and 91.6%, respectively. In contrast, the hydrogenolysis of PP (bottle) and PP needs a longer reaction time, which should be attributed to the large steric effect by these side methyl groups.[16] In addition, the products distribution of PP hydrogenolysis exhibit the high selectivity of liquid products, which further means the source of this selectivity is strong hydrogenation capability in catalyst rather than optimization of reaction condition (Fig. S14). Importantly, we also tested catalytic performance of mixed polyolefin with a mass ratio of LDPE and PP as 2:1, which is similar to the component of the real-world ethylene propylene elastomer. As a result, the solid conversion and liquid yield are 99.19% and 93%, respectively. The non-solid product distribution is shown in Fig. 5e with a carbon center of C20, and the product distribution is close to that of diesel (C8–C21) and motor oil (C18–C34). Moreover, the recycling of real-life plastics was performed. The hydrogenolysis of black-PP lid produced 92.4% of liquid alkanes and 5.7% of gas (Fig. S15). Briefly, the SMSI effect holds great promise in boosting catalytic activity, tuning product selectivity, and enhancing catalyst stability, as well as superior universality, which all are important prospects for the industrial hydrogenolysis of polyolefins.

4. Conclusion

Summarily, we have systematically investigated the effects of classic SMSI on the hydrogenolysis of polyolefins by constructing a Ru/TiO$_2$ catalyst system. The SMSI in Ru/TiO$_2$ catalyst induced the electron transfer from the support to Ru, thus modulating the electronic structures of these loaded Ru NPs. With increased SMSI effect, the Ru NPs showed an electron-rich state, which significantly facilitated the hydrogenation and desorption steps while having little effect on dehydrogenation and cracking capacity. This unique electronic structure resulted in a remarkable enhancement in liquid fuel yield and a decrease of low-value gas products. In detail, under similar solid conversions of nearly 100%, the Ru/TiO$_2$-H600 with the strongest MSI effect had the highest liquid yield of 89.4% with a low gas yield of 8.65%. Moreover, the optimized catalyst showed high efficiency, selectivity and stability for upcycling different types of polyolefins and commercial plastic waste, indicating its great potential for addressing the practical challenge of waste plastic management and environmental conservation. In fact, MSI effect encompassed various factors such as interface effects, geometric effect, in addition to the SMSI. Thus, investigating these MSI effect may provide valuable insights into the reason behind the excellent performance. More significantly, unveiling the structure-performance relationship in polyolefin hydrogenolysis and promote the fundamental research for waste plastic upcycling may be more meaningful. Therefore, by investigating the multifaceted MSI effect and its impact on catalytic performance, we can uncover important insights that advance our knowledge in the field and pave the way for innovative solutions in waste plastic valorization.

Supporting information

The Supporting information is available free of charge. Detailed experimental and computational methods; TEM images and corresponding size distributions; XRD, NAP-XPS spectra and results of Ru/TiO$_2$-HX catalysts; catalytic performance of Ru/TiO$_2$-HX for polyolefin, *n*-hexadecane hydrogenolysis; and DFT calculation results.

CRediT authorship contribution statement

Weilin Tu: Investigation, Writing – original draft. **Mingyu Chu:** Investigation, Writing – original draft. **Xianpeng Wang**: Simulation, Writing – original draft. **Xuchun Wang:** Characterizations, Data curation. **Yifan Li:** Characterizations, Data curation. **Wenxiu Yang:** Investigation. **Muhan Cao:** Writing – review & editing. Lu Wang: Simulation, Writing – review & editing. **Youyong Li:** Writing – review & editing. **Tsun-Kong Sham:** Writing – review & editing. **Yi Cui:** Characterizations, Writing – review & editing. **Qiao Zhang:** Writing – review & editing. **Jinxing Chen:** Conceptualization, Supervision. Weilin Tu, Mingyu Chu and Xianpeng Wang contributed equally to this work.

Declaration of Competing Interest

The authors declare that they have no known competing financial interests or personal relationships that could have appeared to influence the work reported in this paper.

Data Availability

The data that support the findings of this study are available from the corresponding author upon reasonable request.

Acknowledgments

Appendix A. Supporting information

Supplementary data associated with this article can be found in the online version at doi:10.1016/j.apcatb.2023.123122.

References

[1] X.Q. Jia, C. Qin, T. Friedberger, Z.B. Guan, Z. Huang, Efficient and selective degradation of polyethylenes into liquid fuels and waxes under mild conditions, Sci. Adv. 2 (2016), e150159.

[2] J.R. Jambeck, R. Geyer, C. Wilcox, T.R. Siegler, M. Perryman, A. Andrady, R. Narayan, K.L. Law, Plastic waste inputs from land into the Ocean, Science 347 (2015) 768–771.

[3] S.B. Liu, P.A. Kots, B.C. Vance, A. Danielson, D.G. Vlachos, Plastic waste to fuels by hydrocracking at mild conditions, Sci. Adv. 7 (2021) eabf8283.

[4] J.M. Garcia, M.L. Robertson, The future of plastics recycling chemical advances are increasing the proportion of polymer waste that can be recycled, Science 358 (2017) 870–872.

[5] R. Geyer, J.R. Jambeck, K.L. Law, Production, use, and fate of all plastics ever made, Sci. Adv. 3 (2017), e1700782.

[6] C.W.S. Yeung, J.Y.Q. Teo, X.J. Loh, J.Y.C. Lim, Polyolefins and polystyrene as chemical resources for a sustainable future: challenges, advances, and prospects, ACS Mater. Lett. 3 (2021) 1660–1676.

[7] L.D. Ellis, N.A. Rorrer, K.P. Sullivan, M. Otto, J.E. McGeehan, Y. Román-Leshkov, N. Wierckx, G.T. Beckham, Chemical and biological catalysis for plastics recycling and upcycling, Nat. Catal. 4 (2021) 539–556.

[8] S.R. Nicholson, N.A. Rorrer, A.C. Carpenter, G.T. Beckham, Manufacturing energy and greenhouse gas emissions associated with plastics consumption, Joule 5 (2021) 673–686.

[9] A. Rahimi, J.M. García, Chemical recycling of waste plastics for new materials production, Nat. Rev. Chem. 1 (2017) 0046.

[10] J. Zheng, S. Suh, Strategies to reduce the global carbon footprint of plastics, Nat. Clim. Change 9 (2019) 374–378.

[11] M. Chu, Y. Liu, X. Lou, Q. Zhang, J. Chen, Rational design of chemical catalysis for plastic recycling, ACS Catal. 12 (2022) 4659–4679.

[12] J.E. Rorrer, G.T. Beckham, Y. Roman-Leshkov, Conversion of polyolefin waste to liquid alkanes with ru-based catalysts under mild conditions, JACS Au 1 (2021) 8–12.

[13] C. Wang, T. Xie, P.A. Kots, B.C. Vance, K. Yu, P. Kumar, J. Fu, S. Liu, G. Tsilomelekis, E.A. Stach, W. Zheng, D.G. Vlachos, Polyethylene hydrogenolysis at mild conditions over ruthenium on tungstated Zirconia, JACS Au 1 (2021) 1422–1434.

[14] J.E. Rorrer, C. Troyano-Valls, G.T. Beckham, Y. Román-Leshkov, Hydrogenolysis of polypropylene and mixed polyolefin plastic waste over Ru/C to produce liquid alkanes, ACS Sustain. Chem. Eng. 9 (2021) 11661–11666.

[15] C. Jia, S. Xie, W. Zhang, N.N. Intan, J. Sampath, J. Pfaendtner, H. Lin, Deconstruction of high-density polyethylene into liquid hydrocarbon fuels and lubricants by hydrogenolysis over Ru catalyst, Chem. Catal. 1 (2021) 437–455.

[16] Y. Nakaji, M. Tamura, S. Miyaoka, S. Kumagai, M. Tanji, Y. Nakagawa, T. Yoshioka, K. Tomishige, Low-temperature catalytic upgrading of waste polyolefinic plastics into liquid fuels and waxes, Appl. Catal. B 285 (2021), 119805.

[17] L. Chen, L.C. Meyer, L. Kovarik, D. Meira, X.I. Pereira-Hernandez, H. Shi, K. Khivantsev, O.Y. Gutiérrez, J. Szanyi, Disordered, sub-nanometer Ru structures on CeO2 are highly efficient and selective catalysts in polymer upcycling by hydrogenolysis, ACS Catal. 12 (2022) 4618–4627.

[18] P.A. Kots, S. Liu, B.C. Vance, C. Wang, J.D. Sheehan, D.G. Vlachos, Polypropylene plastic waste conversion to lubricants over Ru/TiO2 catalysts, ACS Catal. 11 (2021) 8104–8115.

[19] L. Chen, Y. Zhu, L.C. Meyer, L.V. Hale, T.T. Le, A. Karkamkar, J.A. Lercher, O. Y. Gutiérrez, J. Szanyi, Effect of reaction conditions on the hydrogenolysis of polypropylene and polyethylene into gas and liquid alkanes, React. Chem. Eng. 7 (2022) 844–854.

[20] B.C. Vance, P.A. Kots, C. Wang, Z.R. Hinton, C.M. Quinn, T.H. Epps, L.T.J. Korley, D.G. Vlachos, Single pot catalyst strategy to branched products via adhesive isomerization and hydrocracking of polyethylene over platinum tungstated zirconia, Appl. Catal. B Environ. 299 (2021).

[21] S. Chen, A. Tennakoon, K.-E. You, A.L. Paterson, R. Yappert, S. Alayoglu, L. Fang, X. Wu, T.Y. Zhao, M.P. Lapak, M. Saravanan, R.A. Hackler, Y.-Y. Wang, L. Qi, M. Delferro, T. Li, B. Lee, B. Peters, K.R. Poeppelmeier, S.C. Ammal, C.R. Bowers, F. A. Perras, A. Heyden, A.D. Sadow, W. Huang, Ultrasmall amorphous zirconia nanoparticles catalyse polyolefin hydrogenolysis, Nat. Catal. 6 (2023) 161–173.

[22] J. Wei, J. Liu, W. Zeng, Z. Dong, J. Song, S. Liu, G. Liu, Catalytic hydroconversion processes for upcycling plastic waste to fuels and chemicals, Catal. Sci. Technol. 13 (2023) 1258–1280.

[23] M. Chu, W. Tu, S. Yang, C. Zhang, Q. Li, Q. Zhang, J. Chen, Sustainable chemical upcycling of waste polyolefins by heterogeneous catalysis, SusMat 2 (2022) 161–185.

[24] F. Zhang, M.H. Zeng, R.D. Yappert, J.K. Sun, Y.H. Lee, A.M. LaPointe, B. Peters, M. M. Abu-Omar, S.L. Scott, Polyethylene Upcycling to Long-Chain Alkylaromatics by Tandem Hydrogenolysis/Aromatization, Science 370 (2020) 437–441.

[25] Y. Nakagawa, S.I. Oya, D. Kanno, Y. Nakaji, M. Tamura, K. Tomishige, Regioselectivity and reaction mechanism of Ru-catalyzed hydrogenolysis of squalane and model alkanes, ChemSusChem 10 (2017) 189–198.

[26] M. Tamura, S. Miyaoka, Y. Nakaji, M. Tanji, S. Kumagai, Y. Nakagawa, T. Yoshioka, K. Tomishige, Structure-activity relationship in hydrogenolysis of polyolefins over Ru/support catalysts, Appl. Catal. B-Environ. 318 (2022) 121870.

[27] W.T. Lee, A. van Muyden, F.D. Bobbink, M.D. Mensi, J.R. Carullo, P.J. Dyson, Mechanistic classification and benchmarking of polyolefin depolymerization over silica-alumina-based catalysts, Nat. Commun. 13 (2022) 4850.

[28] P.A. Kots, T. Xie, B.C. Vance, C.M. Quinn, M.D. de Mello, J.A. Boscoboinik, C. Wang, P. Kumar, E.A. Stach, N.S. Marinkovic, L. Ma, S.N. Ehrlich, D.G. Vlachos, Electronic modulation of metal-support interactions improves polypropylene hydrogenolysis over ruthenium catalysts, Nat. Commun. 13 (2022) 5186.

[29] S.J. Tauster, S.C. Fung, R.L. Garten, Strong metal-support interactions. Group 8 noble metals supported on titanium dioxide, J. Am. Chem. Soc. 100 (1978) 170–175.

[30] S.J. Tauster, S.C. Fung, Strong metal-support interactions: occurrence among binary oxides of groups IIA–VB, J. Catal. 55 (1978) 29–35.

[31] E.W. Zhao, H. Zheng, K. Ludden, Y. Xin, H.E. Hagelin-Weaver, C.R. Bowers, Strong metal–support interactions enhance the pairwise selectivity of parahydrogen addition over Ir/TiO2, ACS Catal. 6 (2016) 974–978.

[32] T.W. van Deelen, C. Hernández Mejía, K.P. de Jong, Control of metal-support interactions in heterogeneous catalysts to enhance activity and selectivity, Nat. Catal. 2 (2019) 955–970.

[33] G. Ou, Y. Xu, B. Wen, R. Lin, B. Ge, Y. Tang, Y. Liang, C. Yang, K. Huang, D. Zu, R. Yu, W. Chen, J. Li, H. Wu, L.M. Liu, Y. Li, Tuning defects in oxides at room temperature by lithium reduction, Nat. Commun. 9 (2018) 1302.

[34] J. Zhang, H. Wang, L. Wang, S. Ali, C. Wang, L. Wang, X. Meng, B. Li, D.S. Su, F. S. Xiao, Wet-chemistry strong metal-support interactions in titania-supported Au catalysts, J. Am. Chem. Soc. 141 (2019) 2975–2983.

[35] Y. Zhang, X. Yang, X. Yang, H. Duan, H. Qi, Y. Su, B. Liang, H. Tao, B. Liu, Chen, X. Su, Y. Huang, T. Zhang, Tuning reactivity of fischer-tropsch synthesis by regulating TiOx overlayer over Ru/TiO2 nanocatalysts, Nat. Commun. 11 (2020) 3185.

[36] Y. Zhang, X. Su, L. Li, H. Qi, C. Yang, W. Liu, X. Pan, X. Liu, X. Yang, Y. Huang, T. Zhang, Ru/TiO2 catalysts with size-dependent metal/support interaction for tunable reactivity in Fischer–Tropsch synthesis, ACS Catal. 10 (2020) 12967–12975.

[37] X. Li, J. Lin, L. Li, Y. Huang, X. Pan, S.E. Collins, Y. Ren, Y. Su, L. Kang, X. Liu, Y. Zhou, H. Wang, A. Wang, B. Qiao, X. Wang, T. Zhang, Controlling CO2 hydrogenation selectivity by metal-supported electron transfer, Angew. Chem. Int. Ed. 59 (2020) 19983–19989.

[38] M. Chu, Q. Pan, W. Bian, Y. Liu, M. Cao, C. Zhang, H. Lin, Q. Zhang, Y. Xu, Strong metal–support interaction between palladium and gallium oxide within monodisperse nanoparticles: self-supported catalysts for propyne semi-hydrogenation, J. Catal. 395 (2021) 36–45.

[39] L. Xu, J. Yang, Size and shape-controlled synthesis of Ru nanocrystals, Phys. Sci. Rev. (2018) 199–278.

[40] L. Wang, L. Wang, X. Meng, F.S. Xiao, New strategies for the preparation of sinter-resistant metal-nanoparticle-based catalysts, Adv. Mater. 31 (2019), e1901905.

[41] P. Panagiotopoulou, D.I. Kondarides, Effects of alkali promotion of TiO2 on the chemisorptive properties and water–gas shift activity of supported noble metal catalysts, J. Catal. 267 (2009) 57–66.

[42] Y. Zhan, C. Zhou, F. Jin, C. Chen, L. Jiang, Ru/TiO2 catalyst for selective hydrogenation of benzene: effect of surface hydroxyl groups and spillover hydrogen, Appl. Surf. Sci. 525 (2020).

[43] G.C. Bond, A.D. Hooper, Modification of ruthenium catalysts for alkane hydrogenolysis, Appl. Catal. A Gen. 191 (2000) 69–81.

[44] R. Burch, G.C. Bond, R.R. Rajaram, Hydrogenolysis of alkanes. Part 3.—Hydrogenolysis of n-hexane and methylcyclopentane over variously treated Ru/TiO2 catalysts, J. Chem. Soc. Faraday Trans. 1 Phys. Chem. Condens. Ph. 82 (1986) 1985–1998.

[45] A.S. Almithn, D.D. Hibbitts, Impact of metal and heteroatom identities in the hydrogenolysis of C–X Bonds (X = C, N, O, S, and Cl), ACS Catal. 10 (2020) 5086–5100.

[46] J.J. Sattler, J. Ruiz-Martinez, E. Santillan-Jimenez, B.M. Weckhuysen, Catalytic dehydrogenation of light alkanes on metals and metal oxides, Chem. Rev. 114 (2014) 10613–10653.

[47] D.W. Flaherty, D.D. Hibbitts, E. Iglesia, Metal-catalyzed C-C bond cleavage in alkanes: effects of methyl substitution on transition-state structures and stability, J. Am. Chem. Soc. 136 (2014) 9664–9676.

[48] S. Zhang, Z. Xia, T. Ni, Z. Zhang, Y. Ma, Y. Qu, Strong electronic metal-support interaction of Pt/CeO2 enables efficient and selective hydrogenation of quinolines at room temperature, J. Catal. 359 (2018) 101–111.

[49] G. Celik, R.M. Kennedy, R.A. Hackler, M. Ferrandon, A. Tennakoon, S. Patnaik, A. M. LaPointe, S.C. Ammal, A. Heyden, F.A. Perras, M. Pruski, S.L. Scott, K. Poeppelmeier, A.D. Sadow, M. Delferro, Upcycling single-use polyethylene into high-quality liquid products, ACS Cent. Sci. 5 (2019) 1795–1803.

[50] W.-T. Lee, F.D. Bobbink, A.P. van Muyden, K.-H. Lin, C. Corminboeuf, R.R. Zamani, P.J. Dyson, Catalytic hydrocracking of synthetic polymers into grid-compatible gas streams, Cell Rep. Phys. Sci. 2 (2021) 100332.